Quantitative Mapping of the Elastic Modulus of Soft Materials with HarmoniX and Peak Force QNM AFM Modes

ARTICLE *in* LANGMUIR · OCTOBER 2012

Impact Factor: 4.46 · DOI: 10.1021/la302706b · Source: PubMed

Langmuir

Article

pubs.acs.org/Langmuir

Quantitative Mapping of the Elastic Modulus of Soft Materials with HarmoniX and PeakForce QNM AFM Modes

Maxim E. Dokukin[†] and Igor Sokolov*[,†,‡]

[†]Department of Physics and [‡]Nanoengineering and Biotechnology Laboratories Center (NABLAB), Clarkson University, Potsdam, New York 13699-5820, United States

ABSTRACT: The modulus of elasticity of soft materials on the nanoscale is of interest when studying thin films, nanocomposites, and biomaterials. Two novel modes of atomic force microscopy (AFM) have been introduced recently: HarmoniX and PeakForce QNM. Both modes produce distribution maps of the elastic modulus over the sample surface. Here we investigate the question of how quantitative these maps are when studying soft materials. Three different polymers with a macroscopic Young's modulus of 0.6−0.7 GPa (polyurethanes) and 2.7 GPa (polystyrene) are analyzed using these new modes. The moduli obtained are compared to the data measured with the other commonly used techniques, dynamic mechanical analyzer (DMA), regular AFM, and nanoindenter. We show that the elastic modulus is overestimated in both the HarmoniX and PeakForce QNM modes when using regular sharp probes because of excessively overstressed material in the samples. We further demonstrate that both AFM modes can work in the linear stress−strain regime when using a relatively dull indentation probe (starting from ∼210 nm). The analysis of the elasticity models to be used shows that the JKR model should be used for the samples considered here instead of the DMT model, which is currently implemented in HarmoniX and PeakForce QNM modes. Using the JKR model and∼240 nm AFM probe in the PeakForce QNM mode, we demonstrate that a quantitative mapping of the elastic modulus of polymeric materials is possible. A spatial resolution of ∼50 nm and a minimum 2 to 3 nm indentation depth are achieved.

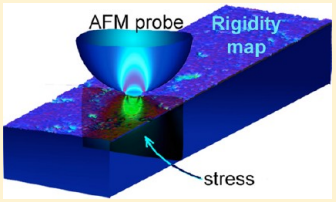

INTRODUCTION

The mechanics of soft materials on the nanoscale is important to the study of nanoheterogeneous materials, such as nanocomposites, multiphased polymers, biomaterials, biological cells, and tissues. For example, the study of nanomechanical properties of polymeric polishing pads is important in the semiconductor industry.[1−3] The superior properties of bionanocomposite materials, for example, abalone shell, have been known for decades whereas its nanomechanical properties were studied just recently.[4] Recent studies of the mechanics of cells on the nanoscale revealed their correlation with a number of diseases and even aging[5−10] and therefore could be used for diagnostic purposes.

Probe-based indentation is a versatile method for studying local mechanical property of materials. It covers dimensions ranging from the nanoscale to the macroscale.[11,12] This method has been used for a wide variety of systems such as homogeneous[13] and composite materials,[14−16] films,[16−22] and live organisms.[7,23,24] There are two major probe indentation techniques currently available: nanoindenter and atomic force microscopy (AFM). Both techniques allow the recording of force−penetration (or hereafter force−indentation) curves. Nanoindenters are nowadays standard instruments used to study the mechanics of materials on the nanoscale. Nonetheless, AFM has been widely used to probe nanomechanical properties for the last 20 years.[19,25−28] When we measure rigid materials, nanoindenting using a nanoindenter is a more convenient and typically more accurate method than AFM. AFM is more preferable when studying soft materials[29] because it can operate at smaller forces and consequently smaller deformations than can nanoindenters.

Atomic force microscopy (AFM) allows the studying of the morphology of soft materials, in particular, polymers and biomaterials.[27,30] Several AFM techniques allow not only the collection of information about surface geometry and phase separation[31,32] but also the recording of mechanical,[19,33−36] electrical,[37−39] and piezoelectrical,[40] magnetic,[41] and chemical[2] properties of sample surfaces. However, quantitative mechanical mapping with resolution comparable to that of the topographical images was not possible with the conventional phase and force modulation imaging techniques.[42,43] The most accurate methods of acquiring quantitative mechanical properties of polymer samples were nanoindentation (using a nanoindenter) and force volume AFM imaging.[19,33,36,44,45] Poor lateral resolution and the extensive time required to obtain a complete map of the surface are the disadvantages of these techniques.

Recently introduced HarmoniX and PeakForce QNM AFM modes[46−48] have allowed the mapping of the elastic modulus of a sample surface with high spatial resolution and as fast as a regular tapping AFM imaging. In both of these techniques, the elastic modulus is derived from the force−indentation curves (by using the Derjaguin−Muller−Toporov (DMT) model[49]). Ideologically, these modes, in particular, PeakForce QNM, are the further developments of the previously known pulsed

Received: July 5, 2012
Revised: October 24, 2012
Published: October 31, 2012

force[50,51] and contact resonance modes.[52] Both HarmoniX and PeakForce modes are capable of working with small (up to <0.1 nN for PeakForce QNM and <5 nN for HarmoniX) load forces and with indentation depths that are as small as 1 nm.[53,54] It is still a serious challenge for both techniques to make quantitative measurements on soft viscoelastic materials on the nanoscale.[36,55−60] To make the quantitative measurements, one needs to perform the cantilever calibration and identify the point of contact and then measure precise probe geometry, the cantilever spring constant, and sample creep.[61] The accuracy of the new AFM methods has not yet been carefully investigated for the case of soft materials.

A somewhat similar problem of quantitative measurements of mechanical properties of polymers has recently been studied when using AFM.[29] It was shown that a typical sharp AFM probe precludes obtaining the correct elastic modulus. Specifically, the modulus was dependent on the indentation depth. This is a broadly observed phenomenon in both AFM- and nanoindenter-based experiments when measuring the elastic properties of supposed-to-be-homogeneous soft materials. Typically, the modulus reaches its bulk (the macroscopic Young's modulus) value only when the indentation depth becomes relatively large.[19,21,56,59,60,62−67] The overestimation of the elastic modulus was found to be model-independent when different elastic models were used.[19,21,65,68] Moreover, the depth-dependent behavior was observed when using an indenter precalibrated with a reference sample,[60] using relative rather than absolute measurements,[69] utilizing corrections of the projection contact area,[69,70] and taking the creep into account.[71] The results of ref 29 showed that the skin effect could be an artifact due to using an excessively sharp probe and sometimes ignoring adhesion between the probe and surface of interest. It was demonstrated that after using a duller probe and taking into account adhesion (through DMT[49] and the Johnson−Kendall−Roberts (JKR)[72] model) the macroscopic Young's modulus of elasticity was observed starting from an indentation of 2 to 3 nm with no further depth dependence. Because the HarmoniX and PeakForce QNM AFM modes are just faster ramping realizations of the study in ref 29, it is interesting to do a similar study for these new AFM modes.

Here we investigate the accuracy of the HarmoniX and PeakForce QNM AFM modes in measuring the mechanics of soft materials by using the example of three different polymers with macroscopic Young's moduli of 0.6 to 0.7 GPa (polyurethanes) and 2.8 GPa (polystyrene). The measured values of the elastic moduli are compared to those obtained with the other commonly used techniques: the dynamic mechanical analyzer (DMA) and the nanoindenter. We show that the elastic modulus is overestimated in both HarmoniX and PeakForce QNM modes if one uses regular sharp AFM probes. We further demonstrate that the correct macroscopic Young's modulus is robustly measured when using a relatively dull indentation probe and taking adhesion into account (JKR model).

EXPERIMENTAL METHODS

Samples. Two kinds of polyurethane (JR111 and OXP4000, Rodel/Dow Chemical, DE) and polystyrene samples were used in this study. The polyurethane samples were cut from a specimen prepared by casting polyurethane during thermosetting on a highly polished hard-drive disk surface. The created flat surface is suitable for study with the AFM and indentation techniques. Polystyrene samples were cut out of a crystal-grade polystyrene Petri dish (BD Falcon). Before measurements, all samples were washed in high-purity ethanol (Sigma-Aldrich) and ultrapure water (Millipore, Inc.) and then dried under nitrogen. For the indentation and AFM measurements, 7 mm × 7 mm coupon samples with a thickness of 0.5−1.2 mm were mounted on metallic coins using a small amount of epoxy adhesive. The samples for the DMA study had a length, width, and thickness of 17.5, 10, and 0.5−1.2 mm, respectively.

DMA. The macroscopic static elastic moduli were measured using a TA Instruments Q800 dynamic mechanical analyzer (DMA). The quasistatic loading mode was employed. Specifically, the Young's modulus was measured (the Poisson ratios were taken from the literature[73−75] (0.38 for polystyrene and 0.4 for polyurethane). The sample was clamped on both sides inside the single cantilever flexed on one side (the so-called cantilever bending mode). All measurements were performed in controlled force/strain mode using the standard 17.5 mm single cantilever. Samples were loaded with a constant force ramp of 3 N/min up to a maximum force of 18 N. The study was conducted at room temperature of 22−24 °C. Freshly cut samples were used for each measurement to avoid errors from plastic deformation. The bulk (macroscopic) values of the elastic modulus were calculated from the slope of the stress/strain curve at strains smaller than 0.5%.

Nanoindenter. A Hysitron TI 950 TriboIndenter indentation system (Hysitron Inc., Minneapolis, MN) was used to perform indentations and record force−displacement curves at the polymer samples. Two types of indentation probes were used: a standard Berkovich-type indenter with a total included angle of 142.35° and a radius of curvature of 150 nm and a nonimaging conospherical probe. The shape of the conospherical probe was provided by the manufacturer (indicating that the apex is close to the ideal sphere with a radius of 108 μm). An evaluation of the shape of the Berkovich probe was performed by analyzing a set of 100 load−penetration curves on a standard quartz sample with load forces of 50−12 000 μN. A standard calibration procedure, which included the load−frame compliance, was performed before each experiment.

All samples were tested in load-control mode. Indentations in three different regions were performed for each sample. To minimize the viscoelastic response, the pattern of a three-segment experiment was used with loading and unloading times of 5 s and holding at the maximum load for 10 s. The creep drift in each indentation experiment was ≤0.2 nm/s. All experiments were performed at room temperature (22−24 °C) and a relative humidity of 40−60%. The elastic modulus was calculated from the unloading part of load−penetration curves using the standard Oliver−Pharr method.[45,76]

AFM HarmoniX and PeakForce QNM. To record surface topology and elastic modulus maps, HarmoniX and PeakForce QNM AFM modes[46−48] together with Nanoscope Dimension 3100 and Bioscope Catalyst (Bruker Nano/Veeco, Inc.) AFMs were used. A Nanoscope V controller and Nanoscope software versions 7.3 and 8.1 were utilized. All measurements were made under ambient conditions at room temperature and a relative humidity of 40−60%. In both cases, the standard cantilever holders for operation in air were used.

All quantitative measurements were performed using either standard RTESP (for PeakForce QNM) and HMX AFM probes (for HarmoniX, both from Veeco/Bruker Instruments) or specially prepared hemispherical dull probes. Hemispherical dull probes (dull probes hereafter) were made from RTESP (Veeco/Bruker Instruments) probes by annealing in air at 1200 °C for 1−5 h.[2,29] The radius of all probes was evaluated by scanning the TipCheck sample (TIP001, Aurora NanoDevices, Canada). The obtained height maps were processed through the SPIP 5.1.11 (Image Metrology A/S) and NanoScope Analysis (Bruker) software, both of which allow the characterization of the tip apex using an actual height image by methods similar to the blind reconstruction method.[77] All probes were checked twice: after the pre-indentation on polystyrene with the maximal load and after all measurements. The shape of dull probes was characterized by imaging-reversed grid samples (TGT1, NT-NGT, Russia and TGT01, Micromash, Inc., Estonia). Specifically, images of dull probes were obtained by deconvoluting the reversed-grid height images with the grid asperity shape. The radii of the standard AFM

probes were found to be in the range of 12−25 nm. The two dull probes used in this work had a geometry close to an ideal spherical shape with a radius of curvature of either 240 ± 20 or 340 ± 20 nm.

The spring constant of cantilevers was measured using the thermal tuning method[78,79] and the reference cantilever method.[80] When the latter method was used, several measurements were done as a function of the position on the reference cantilever to minimize the error in calculation of the unknown spring constant.[81,82] The spring constant of cantilevers used in this work ranged from 35−45 N/m for RTESP and 3−5 N/m for HMX probes. The spatial sensitivity of the AFM photodetector was calibrated against a clean silicon wafer. The elastic modulus channel for the HarmoniX mode was calibrated by the method based on first principles (known force, amplitude, sensitivity, and radius of the probe). The maximum force during imaging was 25 nN for HarmoniX and 50−100 nN for PeakForce QNM modes. For each sample, the topology and elastic modulus images were collected from five different places over sizes of 5 × 5 and 2 × 2 μm^2 and at a digital resolution of 256 pixels × 256 pixels. The 0.5 Hz scanning rate was used. The vertical oscillation/ramping of the probe was 50−60 and 1 kHz in HarmoniX and PeakForce QNM modes, respectively.

THEORETICAL BASIS

The elastic modulus for all samples measured in AFM experiments was calculated using the DMT model[83] as described below (eq 1). In addition, the force−indentation curves extracted from the PeakForce QNM measurements were processed through the JKR model[84] (eqs 2 and 3a). The Oliver−Pharr model[45,85] (equations 4−7) was used to calculate the elastic modulus using the force−indentation curves collected with the nanoindenter. The DMT and JKR models were used for a spherical indenter. The Oliver−Phar model can work with an indenter of almost arbitrary geometry; it was applied for two different sharp, spherical indenters.

When using the DMT model, we analyzed the force−indentation curves with the help of the following equation

$$F_L(i) = \frac{4}{3}E^*\sqrt{R^*}\,i^{3/2} + F_{\text{pull-off}} \tag{1}$$

where F_L is the load force, E^* is the reduced Young's modulus $E^* = E/(1-\nu^2)$, ν is the Poisson ratio, R^* is the reduced radius $1/R^* = 1/R_{\text{indenter}} + 1/R_{\text{surface}}$, i is the indentation depth, and $F_{\text{pull-off}}$ is the force at the point of pull-off of the AFM probe, or the pull-off force for short. The pull-off force can easily be found from the force−indentation curves. The Poisson ratios for all materials were taken from the literature[73−75] (0.38 for polystyrene and 0.4 for polyurethane).

The JKR model does not have an explicit solution for $F_L(i)$. To fit experimental force−indentation curves, the followed parametric fitting was used

$$i(a) = \frac{a^2}{R^*} - \sqrt{\frac{2\pi a w_{\text{adh}}}{E^*}} \tag{2}$$

$$F_L(a) = \frac{4E^*a^3}{3R^*} - 2\sqrt{2\pi E^* w_{\text{adh}} a^3} \tag{3}$$

where parameter a is the radius of contact and w_{adh} is the adhesion energy (per unit area) of interaction of two flat interfaces made of the materials comprising the AFM probe and sample. It can be calculated by using the following equation:

$$w_{\text{adh}} = -\frac{2}{3}\left(\frac{F_{\text{pull-off}}}{\pi R^*}\right) \tag{3a}$$

In the case of a probe with arbitrary (but known) geometry, the Oliver−Pharr model is utilized.[69,76] In the first step of this model, the unloading part of the force−indentation curve is fitted with the help of a power law

$$F_L(i) = A(i - i_f)^m \tag{4}$$

where A and m are the fitting parameters and i_f is the unloading depth corresponding to zero force when unloading.

In the next step, the contact stiffness S at the maximum load is calculated

$$S = Am(i_{\max} - i_f)^{m-1} \tag{5}$$

where $i_{\max}$ is the indentation at the maximum load.

The indentation depth i_c is calculated using the following equation

$$i_c = i_{\max} - \varepsilon\frac{F_{L\max}}{S} \tag{6}$$

where $F_{L\max}$ is the maximum load force and ε is an empirical constant equal to 0.75 in the case of a spherical indenter and 0.727 in the case of a sharp indenter.[86]

Finally, the elastic modulus is found by using the following equation:

$$E = \frac{1}{2\beta}(1-\nu^2)S\frac{\sqrt{\pi}}{\sqrt{A(i_c)}} \tag{7}$$

Here, $A(i_c)$ is the contact area at the indentation depth i_c and β is an empirical correction factor ($\beta = 1.034$).[86]

The maximum vertical compressive stress $\sigma_{\max}$ in the DMT model is reached at the center of the contact circle at the maximal load ($F_{L\max}$) in the sample indented with a spherical probe. It can be found using the following equation:[87,88]

$$\sigma_{\max\,\text{spherical}} = \frac{3}{2}\frac{F_{L\max} - F_{\text{pull-off}}}{\pi a^2} \tag{8}$$

The maximal shear stress calculated for a sharp probe is[87,88]

$$\sigma_{\max\,\text{conical shear}} = \frac{H}{2(1+\alpha)} \tag{9}$$

Here, a is the contact radius, α is the cone semiangle, and $H = F_{L\max}/A(i_c)$.

In the case of the JKR model, the maximum vertical compressive stress was calculated as follows:[88]

$$\sigma_{\max\,\text{center}} = \frac{3}{2}\frac{F_{L\max}}{\pi a^2} + 2\times\frac{-F_{\text{pull-off}} + \sqrt{F_{L\max}(-F_{\text{pull-off}}) + (-F_{\text{pull-off}})^2}}{\pi a^2} \tag{10}$$

The contact diameter is an important value that can be referred to as the lateral resolution of the indentation method. In the case of the Oliver−Pharr model, the contact diameter is an effective diameter of a circle whose area is equal to the area of the probe at a height (calculated from the apex) equal to the contact depth. (It should be noted that the area at a particular contact depth is found directly when characterizing the probe.) For the other three models, the contact diameter d can be calculated though the following equations:

$$d = 2a = 2\sqrt[3]{\frac{3(F_{L\max} - F_{\text{pull-off}})R^*}{4E^*}} \tag{11}$$

in the case of the DMT model and

dx.doi.org/10.1021/la302706b | Langmuir 2012, 28, 16060−16071

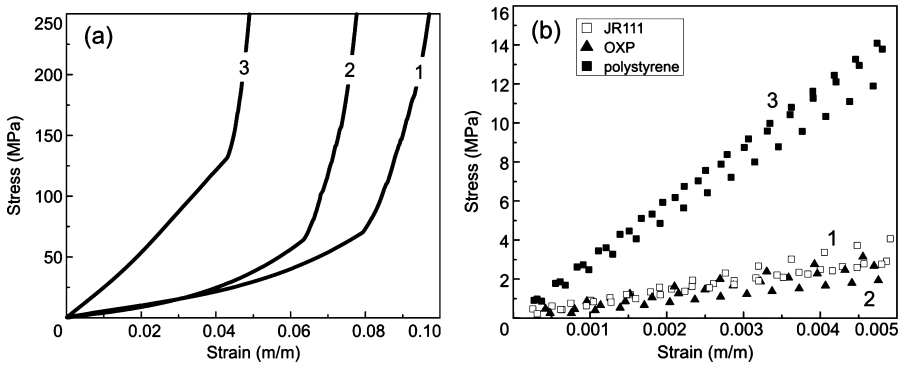

Figure 1. Representative behavior of stress−strain curves collected with DMA. (a) DMA stress−strain curves for JR111 (1), OXP4000 (2), and polystyrene (3). (b) Stress−strain dependence at low strain shown for JR111 (1) (□), OXP4000 (2) (▲), and polystyrene (3) (■) samples.

$$d = 2a = 2 \times \sqrt[3]{\frac{3R^*}{4E^*}\left(F_{\text{Lmax}} - 2F_{\text{pull-off}} + \sqrt{4F_{\text{Lmax}}\left(-F_{\text{pull-off}}\right) + 4\left(-F_{\text{pull-off}}\right)^2}\right)} \quad (12)$$

in the case of the JKR model.

RESULTS AND DISCUSSION

DMA Macroscopic Moduli. It is important to know the macroscopic elastic moduli of measured samples for a quantitative comparison of nanoindentation techniques. The typical stress−strain dependence curves collected by means of DMA on JR111, OXP4000, and polystyrene samples are shown in Figure 1a. One can see that all samples demonstrate linear behavior in the region of small strains and stresses (Figure 1b). However, with increasing applied stress this behavior became clearly nonlinear. The noticeable deviation of the stress−strain curve from linearity can be seen in the region of >∼60 MPa for polyurethane and >∼130 MPa for polystyrene samples. To calculate the macroscopic elastic moduli, we consider only the initial part of the stress−strain curve with strain no more than 0.005 m/m where the stress−strain behavior is linear. The values of the moduli in Figure 2b are 0.63 ± 0.15 GPa for JR111, 0.57 ± 0.14 GPa for OXP4000, and 2.68 ± 0.23 GPa for polystyrene samples.

Nanoindentation. Nanoindentation using a nanoindenter is a standard technique that can be used to study the distribution of mechanical properties over a sample surface. A force−indentation analysis at different indentation depths was also performed. Specifically, 50 force−indentation curves were collected while increasing the maximum load from 50 to 12 000 μN. This was repeated for three different areas on each sample.

Figure 2 shows the results of indentation with the standard Berkovich probe described in the Experimental Methods section. The elastic modulus, the maximum possible stress, and the size of the tip−sample contact were derived with the help of the Oliver−Pharr model (eqs 4−7, 9). The one value of elastic modulus, the maximum possible shear stress, and the size of the tip−sample contacts were calculated from each force−indentation curve.

One can see that the elastic modulus decreases with the increase in indentation depth (i_c) for all polymers (Figure 2a). It is particularly pronounced for the polystyrene sample, in which case the modulus does not reach a constant value. It is important to note that all polymers had a modulus larger than the DMA macroscopic values even at the maximum load

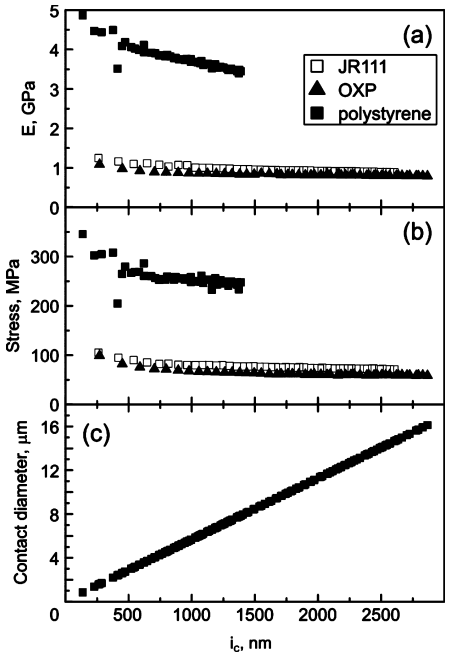

Figure 2. Results of the nanoindenter measurements using the Berkovich probe. Dependence on the indentation depth of (a) the elastic modulus, (b) the maximum stress, and (c) the diameter of contact for OXP4000, JR111, and polystyrene samples.

(maximum indentation depth). The value of the elastic modulus at the plateau for JR111 and OXP4000 is ∼35% greater than the DMA macroscopic measurements. For polystyrene, this difference is about 25% at the maximum indentation depth. It is unlikely that these results come from the changes in polymer structure because all samples were freshly prepared. As we mentioned in the Introduction, similar behavior of the elastic modulus at small indentation depths is common for different polymers; it was found to be model-independent.[19,21,60,62,63,65,68−70] It is worth noting that although the plateau values of the elastic moduli are sufficiently close to the macroscopic ones the area of contact between the probe and sample is on the order of several micrometers. This substantially limits the lateral resolution of this method.

Figure 2b shows the values of the maximum stresses at the sample body as a function of the indentation depth (calculated by using eq 9). One can see that the stress is greater at the small indentation depth. The maximum stress is found to be around 100 MPa for JR111 and OXP4000 and 300 MPa for

dx.doi.org/10.1021/la302706b | Langmuir 2012, 28, 16060−16071

polystyrene. The same stress is related to 0.07−0.09 m/m strain for polyurethane pads and more than 0.05 m/m for polystyrene. Under these stresses, all polymers have a highly nonlinear stress−strain dependence (Figure 1). This results in larger values of the effective elastic modulus. (Note that here we are speaking about the maximum stress. The average value of the stress is lower.)

To decrease substantially or even exclude the problem of nonlinearity during nanoindenter measurements, one can use a duller probe. Here we demonstrate it by using the conospherical indentation probe with a radius of curvature of 108 μm as described in the Experimental Materials section. Figure 3 shows the elastic moduli, the maximum normal

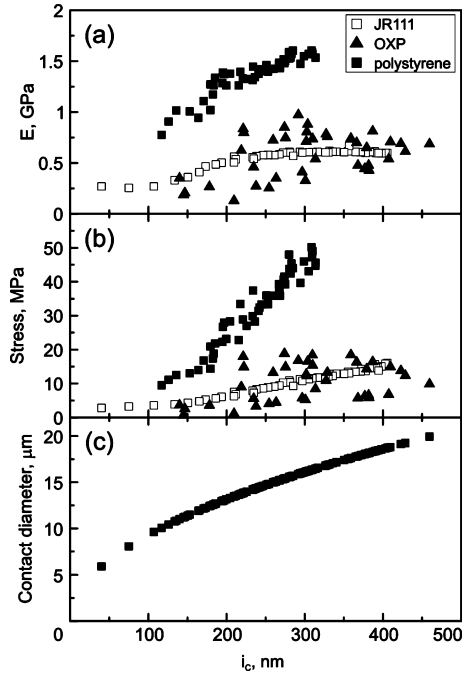

Figure 3. Results of the nanoindenter measurements using a 108 μm radius conospherical probe. Dependence of (a) the elastic modulus, (b) the maximum stress, and (c) the diameter of contact for OXP4000, JR111, and polystyrene samples on the indentation depth.

compressive stress (located at the center of the contact circle evaluated at the maximal load force), and the diameter of contact as a function of the indentation depth. As mentioned previously, each point shown in Figure 3 corresponds to a single force−indentation curve (the curves were collected when the maximum load increases from 50 to 12 000 μN). All points were derived using the Oliver−Pharr model.

One can see from Figure 3c that the maximum stresses are substantially smaller compared to the Berkovich probe and are below the nonlinearity limit. One can conclude that we are now working at the linear stress−strain for all loads. One can also see that the behavior of the elastic modulus has been substantially changed. In contrast to the Berkovich probe, the elastic modulus now increases with the indentation depth. One can see that the elastic modulus reached a plateau at some indentation depth for the polyurethane samples. The plateau reached is very close to the DMA macroscopic values and found to be 0.60 ± 0.02 GPa for JR111 and 0.64 ± 0.18 GPa for OXP4000. The large dispersion of the OXP400 elastic modulus is related to microstructural and topological inhomogeneities of the sample that could be seen in topology and modulus maps (Figure 4 and 5c,d later discussion). Similar to the previous case of the Berkovich probe, the plateau values are reached when the diameter of the probe−sample contact exceeds 10 μm. This limits the resolution of this method as well. The modulus for the polystyrene samples did not reach any constant value even for the maximum indentation force but approached 1.57 GPa, which is 1.7 times smaller than the DMA macroscopic value of polystyrene.

This observed behavior of the elastic modulus can presumably be explained by the surface roughness of the sample. The surface asperities are mostly deformed by such a large probe at the small loads. In the Oliver−Pharr model used here, the area of the contact is derived from the penetration depth. This leads to an overestimation of the contact area for the small penetrations and therefore to an underestimation of the calculated elastic modulus. At the larger deformations, the asperities are completely compressed and the estimated modulus is approaching its macroscopic values. Furthermore, it is presumably the roughness that leads to the much higher variation of the elastic modulus seen in Figure 3 compared to that of the sharper indenter (Figure 2). A larger spread in the elastic modulus values for the OXP sample seen in Figure 3 compared to that for the other two samples occurs because of the greater heterogeneity of the sample material itself.

Let us note that the macroscopic elastic modulus of the polyurethane samples was reached at a depth of ∼300 nm when using the conospherical probe. At the same depth, the elastic modulus measured with the Berkovich probe showed a value greater than 1 GPa. Therefore, we can conclude that the high elastic modulus derived near the sample surface is presumably caused by the nonlinearity in the stress−strain relation rather than by a specific sample structure near the surface. In concluding this section, we stress that the macroscopic modulus was reached at a contact size of ∼15 μm for dull probes. When using the Berkovich probe, the macroscopic modulus was not reached even for the highest contact size of 16 μm.

HarmoniX and PeakForce QNM Elastic Mapping Using a Standard (Sharp) Probe. The same polymer samples as described above were studied with the AFM HarmoniX and PeakForce QNM imaging modes. Both modes showed virtually identical images/maps. Figure 4 shows representative examples of the recorded topography and maps of the elastic modulus for (a, b) JR111, (c, d) OXP4000, and (e, f) polystyrene samples.

The average roughnesses (calculated from the height images) were 3.9, 2.9, and 4.8 nm for OXP4000, JR111, and polystyrene samples, respectively. Flat areas on each sample were used to calculate the values of the elastic modulus. The DMT model was used to calculate elastic modules using the unloading parts of the force curves (eq 1). The average value of the DMT elastic modulus was 2.2 ± 0.3 GPa for JR111 and 1.5 ± 0.5 GPa for OXP4000 samples. This is a factor of 2.5−3.6 greater than the DMA-measured macroscopic moduli. A high variation of the measured modulus presumably comes from the topological roughness and impurities. The latter is more likely for the OXP4000 sample, which is de facto JR111 material with a small number of nanoparticulates added. The value of the elastic modulus of polystyrene was found to be 3.7 ± 0.6 GPa. This value is closer to the macroscopic value (2.7 GPa) but still seems to be overestimated.

There are a number of reasons that the elastic moduli measured in the HarmoniX mode could be higher than the

dx.doi.org/10.1021/la302706b | Langmuir 2012, 28, 16060−16071

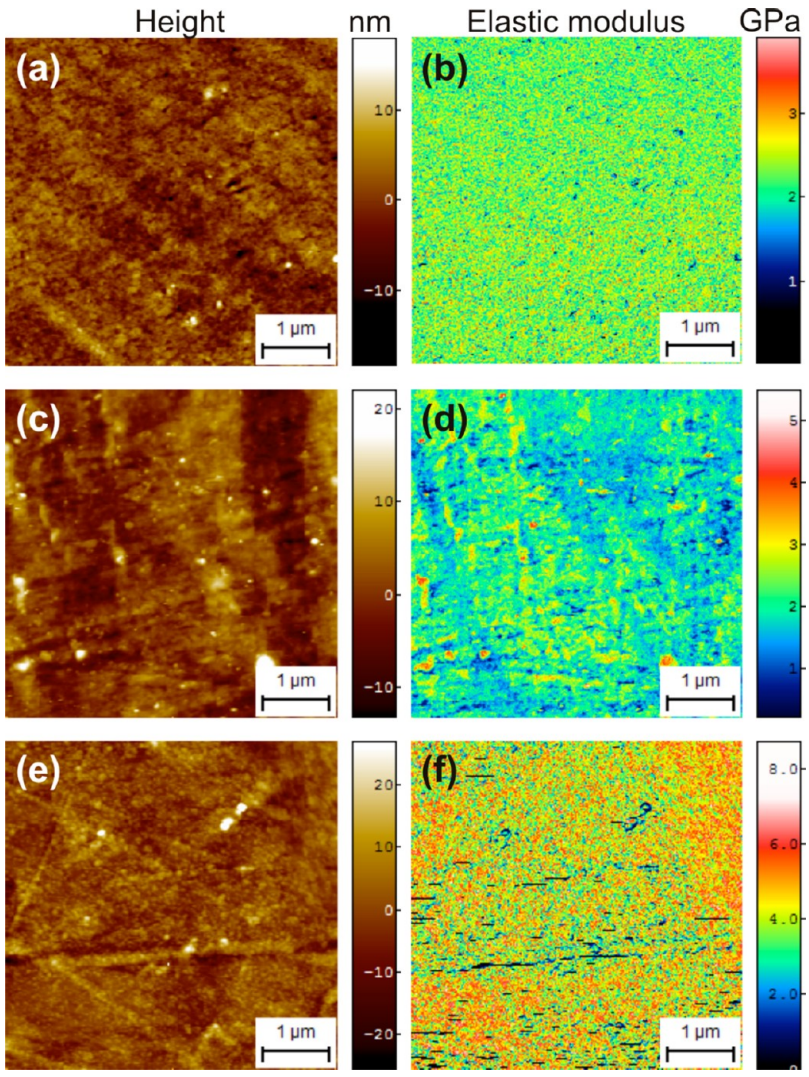

Figure 4. Representative maps of topography and DMT modulus obtained with standard sharp AFM probes when using HarmoniX and PeakForce QNM imaging modes. The images show (a, b) JR111, (c, d) OXP4000, and (e, f) polystyrene samples.

macroscopic value. For instance, it was shown that the elastic modulus could be higher near the surface of some polymers when cross-linking occurred.[89] In our case this is less likely because the samples were freshly prepared. Both fresh samples and the ones tested after some "aging" time showed similar results. Moreover, as was shown in ref 29 the elastic modulus is equal to the macroscopic value and a depth of 2 to 3 nm. The other reason is possible creep-related effects. Because of the very high speed of indentation (the typical interaction time is less than 5×10^{-6} s) it is less likely that we need to consider creep-related increases in the contact area. Next, one can expect to have some change in the elastic modulus as a function of the indentation rate because of the viscoelastic nature of these polymers. This issue will be considered in detail in the next section.

Another reason is the stress−strain nonlinearity for the small indentations, which is clearly seen in Figure 1a for the higher strains. An excessively sharp probe makes it difficult if not impossible to stay within the linearity limits. The maximum stress can be estimated using eq 8 for both HarmoniX and PeakForce QNM modes. The DMT modulus maps shown in Figure 4 were collected when the load force was 18 nN. The average pull-off force during these measurements was found to be around 7 nN. Using the expected value of the elastic modulus to be equal to its macroscopic value of ∼0.6 GPa for JR111 and OXP4000 and 2.7 GPa for polystyrene samples and taking the probe radius to be ∼12−24 nm, we can estimate the maximum normal compressive stress to be within the range of 140−230 MPa for JR111 and OXP4000 and 330−625 MPa for the polystyrene samples. The stress−strain relation for such stress is highly nonlinear (Figure 1). If one still assumed the linear approximation, then the elastic modulus would be noticeably higher. Thus, this may be the reason for the overestimation of the elastic modulus observed in HarmoniX and PeakForce QNM mapping (Figure 4). In the next section, we demonstrate that the use of a dull probe chosen to stay within the linearity limits can indeed result in values of the elastic modulus that are rather close to the macroscopic ones.

PeakForce QNM Using Dull Spherical Probes: The Measured Values Are Close to the Macroscopic Moduli. As was shown above, it is important to stay within the linearity limits of the stress−strain relation to measure the elastic modulus accurately. To decrease the applied maximum stress, one can use a probe with a larger radius. Let us estimate the minimum radius of the probe needed to stay in the linear

dx.doi.org/10.1021/la302706b | *Langmuir* 2012, 28, 16060−16071

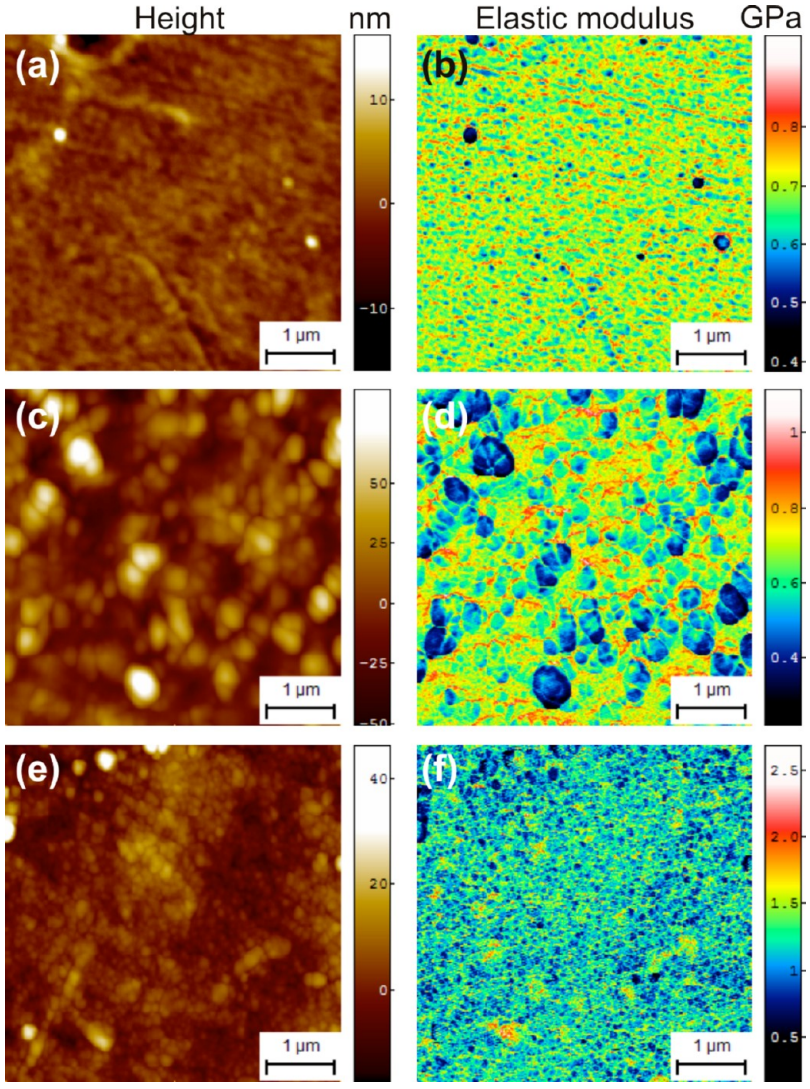

Figure 5. Representative maps of the topography and DMT modulus obtained with dull AFM probes of well-defined spherical geometry when using HarmoniX and PeakForce QNM imaging modes. The images show (a, b) JR111, (c, d) OXP4000, and (e, f) polystyrene samples.

stress−strain regime. Such a radius can be estimated using the following equation[90]

$$R^* = \frac{6w_{adh}E^{*2} + \sqrt{6}\sqrt{\pi E^{*2}F_{Lmax}\sigma_{max}{}^3 + 6w_{adh}{}^2E_2{}^{*4}}}{\pi^2\sigma_{max}{}^3} \quad (13)$$

where $w_{adh} \cong 0.035$ J/m^2 as found from eq 3a.

To keep the maximum stress below 60 MPa in the case of polyurethane samples (with the maximum load force being 50 nN), one can find that the probe radius should not be less than 210 nm for the polyurethane samples. In the case of polystyrene (maximum load of 50 nN and maximum stress of 130 MPa), the minimum probe radius should not be less than 340 nm. Note that this calculation is rather conservative because it relies on the maximum stress. The average stress of the material in the vicinity of the contact is lower. Thus, one can expect a rather accurate result with a reasonably sharper probe.

It is worth noting that the above calculation demonstrates that it is impossible to overcome the nonlinearity by simple decreasing the load force. Physically, this is because of the presence of the adhesion force. From a practical point of view, it is almost impossible to conduct surface rigidity mapping using a very small load force because of an excessively small feedback signal.

To test the conclusion of the above calculations, we prepared dull probes of 240 ± 20 or 340 ± 20 nm to work with the PeakForce QNM AFM mode. (Because of the nontrivial geometry of the cantilevers used in HarmoniX mode, we were unable to prepare the dull probes for the HarmoniX mode.) Figure 5 shows the results of measurements using the PeakForce QNM imaging mode. Close-to-spherical probes with a radius of curvature of 240 ± 20 nm were used. (The results for the 340 nm probe are identical to those of the 240 nm probe within the error of measurement.) Representative maps of the recorded topography and the DMT modulus are presented for JR111 (Figure 5a,b), OXP4000 (Figure 5c,d), and polystyrene (Figure 5e,f) samples. It is worth noting that the spatial resolution in the maps of the elastic modulus is ∼50 nm (Figure 5f). This is in good agreement with the estimation of the area of contact between the probe and sample using eqs 11 and 12.

The maps show some clear artifacts due to nonflat geometry: higher "bumps" demonstrate lower rigidity. This is particular

dx.doi.org/10.1021/la302706b | *Langmuir* 2012, 28, 16060−16071

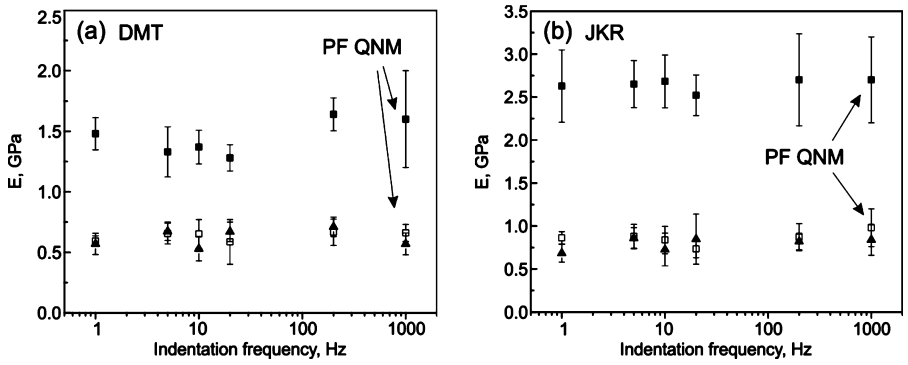

Figure 6. Dependence of the elastic modulus on the indentation rate calculated using (a) DMT and (b) JKR models. JR111 (□), OXP4000 (▲), and polystyrene (■) samples. Elastic moduli at 1000 Hz are the values measured in the PeakForce QNM mode, whereas the rigidity at the other frequencies is measured by using a regular AFM setup. The error bars were calculated on the basis of five measurements in different parts of the sample.

noticeable on the OXP4000 sample. To exclude these artifacts, the elastic modulus was analyzed on the flat parts of the samples only. The average values of the elastic modulus were found to be 0.66 ± 0.07 GPa for JR111, 0.57 ± 0.09 GPa for OXP4000, and 1.6 ± 0.4 GPa for the polystyrene samples. One can see that the elastic moduli of polyurethane samples (JR111 and OXP4000) are in good agreement with the macroscopic values. At the same time, the modulus of polystyrene is substantially smaller than its macroscopic value.

Let us analyze the possible origin of the above underestimation of the elastic modulus of the polystyrene sample. Let us note that the DMT model was used here to obtain the elastic modulus. As was shown in ref 29, the smaller value of the elastic modulus of the polystyrene sample could be obtained because the DMT model could not be applied, so the Johnson–Kendall–Roberts (JKR) model should be used. Because the parameters of the indentation in the PeakForce QNM imaging mode are different than those in the AFM quasi-static indentation mode used in ref 29, let us verify which model is appropriate to use in the present case.

The choice between the JKR and DMT models can be made on the basis of the use of so-called Maugis parameter α,[90,91] which is a dimensionless parameter ranging from 0 to 1 ($\alpha = 1$ corresponds to the JKR case and $\alpha = 0$ corresponds to the DMT case). Maugis parameter α relates to the known Tabor parameter μ_T[92] as follows[91]

$$\alpha = -\frac{50}{51}(e^{250\lambda/231} - 1) \tag{14}$$

where $\lambda = 1.157\ \mu_T = 1.157(w_{adh}^2 R^*/E^{*2}D_0^3)^{1/3}$,[90,91] w_{adh} is the adhesive energy per unit area, R^* is the reduced radius, $E^* = E/(1 - \nu^2)$ is the reduced Young's modulus, D_0 is the interatomic distance between the atoms of the probe and sample at contact, and ν is the Poisson ratio.

To evaluate the Maugis parameter, we specifically used D_0 = 0.16 ± 0.03 nm for the polyurethane–vacuum–silica interaction (JR111 and OXP4000 samples) and D_0 = 0.15 ± 0.01 nm for the polystyrene–vacuum–silica interaction (polystyrene sample).[29] Young's modulus E was taken from the macroscopic modulus measured in the DMA experiments. The adhesive energy w_{adh} was calculated using the data of the AFM indentations with the dull 240 nm probe against the flat part of a sample. The Poisson ratios for all three samples (0.38 for polystyrene and 0.4 for polyurethane) were taken from the literature.[73−75] Using these values, one can estimate the Maugis parameter to be 0.98 for JR111, 0.97 for OXP, and 0.89 for the polystyrene samples. Thus, the use of the JKR model is more appropriate for all samples in this work.

Let us recalculate the values of the elastic modulus obtained in the PeakForce QNM mode with the help of the JKR model. This can be done because the PeakForce QNM mode allows us to save the original force curves for one line of the scanned data. After recalculating the elastic modulus of the polystyrene sample with the JKR model, the value of the elastic modulus was found to be 2.7 ± 0.5 GPa. This is in perfect agreement with the macroscopic value. At the same time, in the case of the JR111 polyurethane sample, the JKR model gives a modulus of 0.98 ± 0.22 GPa, and for the OXP4000 sample, it gives a modulus of 0.84 ± 0.18 GPa. These two moduli are larger than the macroscopic value for the polyurethane samples. The estimated maximum normal compressive stress located at the center of the contact circle for the used 240-nm-radius probes is about 140 MPa for polystyrene and about 50 MPa for JR and OXP. These stresses are fairly close to the nonlinearity limit. Therefore, it is unlikely that the increase is due to the nonlinearity. Let us discuss the last possible reason for the discrepancy of the elastic modulus of polyurethane samples, which is a possible contribution of viscoelasticity.

Possible Contribution of Viscoelasticity. When comparing the results obtained in the PeakForce QNM mode with the macroscopic values, it should be remembered that these are obtained in, strictly speaking, different temporal regimes. The macroscopic values are obtained using quasi-static measurements, whereas the probe in the PeakForce QNM oscillates with a frequency of 1 kHz. Because of the possible viscoelastic response of the samples, these two moduli will be different.

Here we test the influence of the different indentation rates (oscillation frequency) on the elastic modulus derived using the dull probe (240 ± 20 nm in radius). To do that, we measured the force–indentation curves for all three samples used in the PeakForce QNM experiment but using a regular AFM setup. It allows the recording of the force–indentation curves with an oscillation frequency of up to 200 Hz. To match the conditions of the PeakForce QNM experiments, all measurements were made with the same dull probe and with a ramp size of 250 nm. Although we showed that the JKR model should be used in the case of these samples and indentation parameters, we processed the data through both JKR and DMT models to demonstrate that there is virtually no dependence of the elastic modulus on

dx.doi.org/10.1021/la302706b | Langmuir 2012, 28, 16060−16071

Table 1. Summary of the Elastic (Young's) Moduli Derived When Using Various Models, Methods, and Probes[a]

	JR111, GPa	OXP, GPa	PS, GPa	max stress, MPa	contact diameter, nm	depth, nm
macro DMA	0.63 ± 0.15	0.57 ± 0.14	2.68 ± 0.23	~1	~5 × 10^6	n/a
nanoindenter (Berkovich probe, Oliver–Pharr)	0.91 ± 0.02	0.81 ± 0.01	<3.4	~100 (JR, OXP) ~300 (PS)	>8000	>1500
nanoindenter (conospherical probe, Oliver–Pharr)	0.60 ± 0.02	0.64 ± 0.18	>1.57	~20 (JR, OXP) ~50 (PS)	>15 000	>300
AFM HarmoniX/PeakForce QNM (sharp probe, DMT model)	2.2 ± 0.3	1.5 ± 0.5	3.7 ± 0.6	~140–230 (JR, OXP) ~330–625 (PS)	5–10	1–3
AFM PeakForce QNM (dull probe, DMT model)	0.66 ± 0.07	0.57 ± 0.09	1.6 ± 0.4	~50–60 (JR, OXP) ~110–140 (PS)	35–70	2–10
AFM PeakForce QNM (dull probe, JKR model)	0.98 ± 0.22	0.84 ± 0.18	2.7 ± 0.5	~50 (JR, OXP) ~140 (PS)	~50	~3

[a]The elastic moduli derived from indentation experiments are the plateau values (when they weakly depend on indentation). If the plateau was not reached, then the modulus value is given as an inequality. The maximum contact stresses, the contact diameter, and the indentation depth correspond to the elastic modulus presented in the table.

the indentation frequency/speed up to 1 kHz/speed of the PeakForce QNM mode.

As one can see from Figure 6, the elastic moduli calculated using either the DMT or JKR model do not show a noticeable dependence on the indentation rate. Within the variability of the modulus, it virtually remains the same for all range of indentation speeds. Therefore, the higher-than-macroscopic values of the elastic modulus obtained for polyurethane cannot be explained by the viscoelasticity. Thus, the obtained values of the elastic modulus for polyurethane samples can be the true values of the elastic modulus of the polyurethane matrix on the nanoscale.

It should be stressed that the weak dependence of the elastic modulus on frequency observed for three polymeric samples used in this study is simply coincidental. In general, the frequency dependence can be more complicated, in particular, near the glass transition of the polymeric material.

Other Possible Errors. The other possible errors in the calculation of the elastic modulus are worth discussing. We did a similar analysis previously.[29] Here we adjust the analysis of the methods used in this work.

The uncertainty in the indenting probe shape is the one of the main sources of measurement errors in the indentation experiments.[71] This error is minimized in our case because we are using the high-resolution AFM tip-check method to determine the shape of the probe with high accuracy. As an example, the radii of the dull probes used in this work have a maximum error of 10%. According to eqs 1–3a, this results in an error of ~5% in the value of the elastic modulus.

The other errors came from the uncertainty in the determination of the point of contact, the error in measuring the spring constant of the AFM cantilever, the surface and probe roughness, scanner and sample creep, and AFM photodetector nonlinearity.[33,93−95] Here we exclude the AFM photodetector nonlinearity and scanner creep by using the closed-loop scanner and calibrating the photodetector as described by the manufacturer. The roughness of annealed or fresh sharp probes is also very small.[96] The error coming from inaccuracy in the definition of the probe–sample contact point was estimated[29] to be within 10%. The error coming from the uncertainty in the spring constant of the AFM cantilever equals the error in the rigidity modulus (because the rigidity modulus is generally proportional to the load force, which is proportional to the spring constant). It is commonly accepted that the spring constant of the AFM cantilever can be measured with 10–20% error.[59−63] This implies that we should expect 10–20% error in the definition of the elastic modulus. It should be noted that this error, being the same multiplicative factor for all measured moduli, does not change the dependence of the modulus on the indentation depth.

As to the error coming from the creep effect of the sample, it was found that the polymer creep caused an overestimation of the rigidity modulus of up to ~30%.[71,97] This is not sufficient to explain the much higher elastic modulus when measuring with the sharp indenting probe. As to the dull probes, the creep effect can be neglected because we do not observe the hysteresis between loading–unloading force–indentation curves. To summarize, neither of these errors seems to explain the observed discrepancies between the methods analyzed in this work.

Summary of the Results. The results obtained are summarized in Table 1. One can see from the table that the elastic moduli are close to the macroscopic Young's moduli when using the dull probe for both the nanoindenter and AFM techniques, when the stress in the sample material does not exceed the linearity limit.

The values of the elastic moduli derived from the indentation experiments using the nanoindenter are presented as inequalities. This is because the plateau did not reach the maximum possible force used in the nanoindenter. (It is the plateau value that should be used in the value of the modulus according to the manufacturer.) Therefore, the true value of the modulus derived in these experiments should be reached for even higher indentations. The inequality of the modulus is decided on the basis of Figures 2 and 3.

When the AFM indentation is analyzed, the rigidity models that take into account adhesion—the DMT and JKR models—are used. Although the DMT model is in good agreement with the macroscopic values for polyurethane samples, it gives a much smaller modulus for the polystyrene sample. On the contrary, the JKR model determines the elastic modulus more accurately in the case of polystyrene samples. At the same time, this model leads to somewhat overestimated moduli values for polyurethane samples, though the deviation from the macroscopic moduli is within the calculation error. The analysis shows that the JKR model is more appropriate to use for the samples and indentations used in this work. Therefore, we conceive that the results of the PeakForce QNM mode, which

were obtained with the dull probe and processed through the JKR model, represent the true values of the elastic modulus of these polymers on the nanoscale. The small difference in the macroscopic values observed for polyurethane samples could be explained by a sufficient number of defects on the mesoscale in the samples. This is seen through a low optical clearness of the samples. Polystyrene, in contrast, seems to be free of defects as can be seen by its optical transparency.

■ CONCLUSIONS

Here we investigated the ability of two novel AFM modes, HarmoniX and PeakForce QNM, to produce quantitative maps of the elastic modulus. Three different polymers of the macroscopic elastic modulus of 0.6−0.7 GPa (polyurethanes) and 2.7 GPa (polystyrene) were analyzed. The microscopic (Young's) modulus of the polymers was measured for each individual sample using a dynamic mechanical analyzer (DMA). The modulus was also found with the help of a commonly used technique, the nanoindenter.

DMA allowed us to measure not only the elastic modulus but also the limits of the linear relation between stress and strain. We demonstrated that the nanoindenter cannot be reliably used to extract the elastic modulus of the polymers analyzed in this work. A knowledge of the linearity limit allowed us to find that regular sharp AFM probes, which were used in HarmoniX and PeakForce QNM modes, led to stresses that were larger than the linearity limit of the sample. This, in turn, resulted in the overestimation of the elastic moduli for all samples. This overestimation was similar for HarmoniX and PeakForce QNM modes and the nanoindenter when the stress exceeded the linearity limit. We showed that such an overestimation could not be explained by the sample aging near the surface, sample creep, or the viscoelastic response of the samples. We further demonstrated that the nonlinearity could be decreased if not eliminated by using a relatively dull indentation probe (the radius of curvature should be larger than 210 nm). Furthermore, the analysis of the rigidity model to be used showed that the JKR model should be used for the particular samples considered here instead of the DMT model that is currently implemented in HarmoniX and PeakForce QNM modes. Using such probes and models, we demonstrated a quantitative high-resolution mapping of the polymeric materials using the PeakForce QNM mode working with a 240 nm AFM probe. The lateral spatial resolution while working with such a probe was ∼50 nm.

To summarize, a quantitative high-resolution mapping of soft materials with the HarmoniX and PeakForce QNM AFM modes is possible when using a relatively dull probe and the appropriate rigidity model (e.g., ∼240 nm and JKR model for the polymer samples analyzed here). The solution suggested here allows us to measure the true elastic modulus for soft materials in the form of bulk, thin films, nanocomposites, and biological objects using the new HarmoniX and PeakForce QNM AFM modes. The ability to measure the true elastic modulus on the nanoscale at a low indentation depth (∼3 nm) makes it possible to map the elastic modulus with rather high spatial resolution even with a dull probe (up to 50 nm in the present work).

■ AUTHOR INFORMATION

Corresponding Author

*E-mail: isokolov@clarkson.edu. Phone: 1-315-268-2375.

Notes

The authors declare no competing financial interest.

■ ACKNOWLEDGMENTS

The authors are thankful to Bruker AXS Corp. for the HarmoniX Innovation Award and lending the license for the PeakForce QNM mode. Partial funding for this study from NanoScience Solutions (through NSF SBIR award IIP 1214705) and a gift from Xerox Inc. (I.S.) are acknowledged.

■ REFERENCES

(1) Sokolov, I.; Ong, Q. K.; Chechik, N.; James, D. On Direct Measurement of Forces between Cmp Polishing Pand and Abrasive Nanoparticles. *Proceedings of the World Tribology Congress III*; Washington, DC 2005; pp 503−504.

(2) Sokolov, I.; Ong, Q. K.; Shodiev, H.; Chechik, N.; James, D.; Oliver, M. AFM study of forces between silica, silicon nitride and polyurethane pads. *J. Colloid Interface Sci.* **2006**, *300*, 475−481.

(3) Wang, Y. L.; Liu, C.; Chang, S. T.; Tsai, M. S.; Feng, M. S.; Tseng, W. T. Chemical-mechanical polishing of low-dielectric-constant spin-on-glasses: film chemistries, slurry formulation and polish selectivity. *Thin Solid Films* **1997**, *308*, 550−554.

(4) Meyers, M. A.; Lin, A. Y.; Chen, P. Y.; Muyco, J. Mechanical strength of abalone nacre: role of the soft organic layer. *J. Mech. Behav. Biomed. Mater.* **2008**, *1*, 76−85.

(5) Lekka, M.; Laidler, P.; Gil, D.; Lekki, J.; Stachura, Z.; Hrynkiewicz, A. Z. Elasticity of normal and cancerous human bladder cells studied by scanning force microscopy. *Eur. Biophys. J. Biophys. Lett.* **1999**, *28*, 312−316.

(6) Cross, S. E.; Jin, Y. S.; Rao, J.; Gimzewski, J. K. Nanomechanical analysis of cells from cancer patients. *Nat. Nanotechnol.* **2007**, *2*, 780−783.

(7) Iyer, S.; Gaikwad, R. M.; Subba-Rao, V.; Woodworth, C. D.; Sokolov, I. AFM detects differences in the surface brush on normal and cancerous cervical cells. *Nat. Nanotechnol.* **2009**, *4*, 389−393.

(8) Sokolov, I.; Iyer, S.; Subba-Rao, V.; Gaikwad, R. M.; Woodworth, C. D. Detection of surface brush on biological cells in vitro with atomic force microscopy. *Appl. Phys. Lett.* **2007**, *91*, 023902−023901−023903.

(9) Suresh, S. Biomechanics and biophysics of cancer cells. *Acta Mater* **2007**, *55*, 3989−4014.

(10) Sokolov, I.; Iyer, S.; Woodworth, C. D. Recover of elasticity of aged human epithelial cells in-vitro. *Nanomed.: Nanotechnol., Biol. Med.* **2006**, *2*, 31−36.

(11) Cheng, Y. T.; Cheng, C. M. Scaling, dimensional analysis, and indentation measurements. *Mater. Sci. Eng., R* **2004**, *44*, 91−149.

(12) VanLandingham, M. R. Review of instrumented indentation. *J. Res. Natl. Inst. Stand. Technol.* **2003**, *108*, 249−265.

(13) Vlassak, J. J.; Nix, W. D. Measuring the elastic properties of anisotropic materials by means of indentation experiments. *J. Mech. Phys. Solids* **1994**, *42*, 1223−1245.

(14) Hodzic, A.; Kalyanasundaram, S.; Kim, J. K.; Lowe, A. E.; Stachurski, Z. H. Application of nano-indentation, nano-scratch and single fibre tests in investigation of interphases in composite materials. *Micron* **2001**, *32*, 765−775.

(15) An, L.; Chan, H. M.; Padture, N. P.; Lawn, B. R. Damage-resistant alumina-based layer composites. *J. Mater. Res.* **1996**, *11*, 204−210.

(16) Misra, A.; Hirth, J. P.; Hoagland, R. G. Length-scale-dependent deformation mechanisms in incoherent metallic multilayered composites. *Acta Mater.* **2005**, *53*, 4817−4824.

(17) Volinsky, A. A.; Moody, N. R.; Gerberich, W. W. Interfacial toughness measurements for thin films on substrates. *Acta Mater.* **2002**, *50*, 441−466.

(18) Gouldstone, A.; Koh, H. J.; Zeng, K. Y.; Giannakopoulos, A. E.; Suresh, S. Discrete and continuous deformation during nano-indentation of thin films. *Acta Mater.* **2000**, *48*, 2277−2295.

(19) Domke, J.; Radmacher, M. Measuring the elastic properties of thin polymer films with the atomic force microscope. *Langmuir* **1998**, *14*, 3320−3325.
(20) Godovsky, Y. K.; Magonov, S. N. Atomic force microscopy visualization of morphology and nanostructure of an ultrathin layer of polyethylene during melting and crystallization. *Langmuir* **2000**, *16*, 3549−3552.
(21) Dimitriadis, E. K.; Horkay, F.; Maresca, J.; Kachar, B.; Chadwick, R. S. Determination of elastic moduli of thin layers of soft material using the atomic force microscope. *Biophys. J.* **2002**, *82*, 2798−2810.
(22) Sokolov, I.; Subba-Rao, V.; Luck, L. A. Change in rigidity in the activated form of the glucose/galactose receptor from E-coli: a phenomenon that will be key to the development of biosensors. *Biophys. J.* **2006**, *90*, 1055−1063.
(23) A-Hassan, E.; Heinz, W. F.; Antonik, M. D.; D'Costa, N. P.; Nageswaran, S.; Schoenenberger, C. A.; Hoh, J. H. Relative microelastic mapping of living cells by atomic force microscopy. *Biophys. J.* **1998**, *74*, 1564−1578.
(24) Berdyyeva, T. K.; Woodworth, C. D.; Sokolov, I. Human epithelial cells increase their rigidity with ageing in vitro: direct measurements. *Phys. Med. Biol.* **2005**, *50*, 81−92.
(25) Fischer-Cripps, A. C. A review of analysis methods for sub-micron indentation testing. *Vacuum* **2000**, *58*, 569−585.
(26) Lu, Z. X.; Liu, L. T.; Qi, X. R. Development of small interfering RNA delivery system using PEI-PEG-APRPG polymer for antiangiogenic vascular endothelial growth factor tumor-targeted therapy. *Int J Nanomed* **2011**, *6*, 1661−1673.
(27) Fang, T. H.; Chang, W. J.; Tsai, S. L. Nanomechanical characterization of polymer using atomic force microscopy and nanoindentation. *Microelectron. J.* **2005**, *36*, 55−59.
(28) Cho, H. J.; Yoon, I. S.; Yoon, H. Y.; Koo, H.; Jin, Y. J.; Ko, S. H.; Shim, J. S.; Kim, K.; Kwon, I. C.; Kim, D. D. Polyethylene glycol-conjugated hyaluronic acid-ceramide self-assembled nanoparticles for targeted delivery of doxorubicin. *Biomaterials* **2012**, *33*, 1190−1200.
(29) Dokukin, M. E.; Sokolov, I. On the measurements of rigidity modulus of soft materials in nanoindentation experiments at small depth. *Macromolecules* **2012**, *45*, 4277−4288.
(30) Sokolov, I.; Firtel, M.; Henderson, G. S. In situ high-resolution AFM imaging of biological surfaces. *J. Vac. Sci. Technol., B* **1996**, *14*, 674−678.
(31) Tang, Y. W.; Labow, R. S.; Revenko, I.; Santerre, J. P. Influence of surface morphology and chemistry on the enzyme catalyzed biodegradation of polycarbonate-urethanes. *J. Biomater. Sci., Polym. Ed.* **2002**, *13*, 463−483.
(32) Milhiet, P. E.; Giocondi, M. C.; Baghdadi, O.; Ronzon, F.; Le Grimellec, C.; Roux, B. AFM detection of GPI protein insertion into DOPC/DPPC model membranes. *Single Mol.* **2002**, *3*, 135−140.
(33) Butt, H. J.; Cappella, B.; Kappl, M. Force measurements with the atomic force microscope: technique, interpretation and applications. *Surf. Sci. Rep.* **2005**, *59*, 1−152.
(34) DimitriadisE. K.HorkayF.KacharB.MarescaJ.ChadwickR. S.Determination of the Elastic Modulus of Thin Gels Using the Atomic Force Microscope. In *Biophysics of the Cochlea: From Molecules to Models*, Proceedings of the International Symposium, Titisee, Germany, July 27−August 1, 2002; Gummer, A. W., Ed.; World Scientific: River Edge, NJ, 2003; pp 177−178.
(35) Lin, D. C.; Dimitriadis, E. K.; Horkay, F. Elastic modulus maps of soft, rubber-like gels and tissues from AFM nanoindentation. *Biophys. J.* **2007**, 514a−514a.
(36) Tranchida, D.; Kiflie, Z.; Acierno, S.; Piccarolo, S. Nanoscale mechanical characterization of polymers by atomic force microscopy (AFM) nanoindentations: viscoelastic characterization of a model material. *Meas. Sci. Technol.* **2009**, *20*, 095702.
(37) Hane, F.; Moores, B.; Amrein, M.; Leonenko, Z. Effect of SP-C on surface potential distribution in pulmonary surfactant: atomic force microscopy and Kelvin probe force microscopy study. *Ultramicroscopy* **2009**, *109*, 968−973.
(38) Finot, E.; Leonenko, Y.; Moores, B.; Eng, L.; Amrein, M.; Leonenko, Z. Effect of cholesterol on electrostatics in lipid-protein films of a pulmonary surfactant. *Langmuir* **2010**, *26*, 1929−1935.
(39) Dokukin, M.; Olac-Vaw, R.; Guz, N.; Mitin, V.; Sokolov, I. Addressable photocharging of single quantum dots assisted with atomic force microscopy probe. *Appl. Phys. Lett.* **2009**, *95*.
(40) Trolier-McKinstry, S.; Griggio, F.; Yaeger, C.; Jousse, P.; Zhao, D.; Bharadwaja, S. S.; Jackson, T. N.; Jesse, S.; Kalinin, S. V.; Wasa, K. Designing piezoelectric films for micro electromechanical systems. *IEEE Transactions Ultrason., Ferroelectr., Freq. Control* **2011**, *58*, 1782−1792.
(41) Wadas, A.; Grutter, P.; Guntherodt, H. J. Analysis of magnetic bit pattern by magnetic force microscopy. *J. Vac. Sci. Technol., A* **1990**, *8*, 416−420.
(42) Garcia, R.; Perez, R. Dynamic atomic force microscopy methods. *Surf. Sci. Rep.* **2002**, *47*, 197−301.
(43) Sokolov, I. Y. On the limits on spectroscopic ability of afm and interaction between an afm tip and a sample. *Surf. Sci.* **1994**, *311*, 287−294.
(44) Tranchida, D.; Piccarolo, S.; Soliman, M. Nanoscale mechanical characterization of polymers by AFM nanoindentations: Critical approach to the elastic characterization. *Macromolecules* **2006**, *39*, 4547−4556.
(45) Pharr, G. M. Measurement of mechanical properties by ultra-low load indentation. *Mater. Sci. Eng., A* **1998**, *253*, 151−159.
(46) Sahin, O.; Magonov, S.; Su, C.; Quate, C. F.; Solgaard, O. An atomic force microscope tip designed to measure time-varying nanomechanical forces. *Nat. Nanotechnol.* **2007**, *2*, 507−514.
(47) Schon, P.; Bagdi, K.; Molnar, K.; Markus, P.; Pukanszky, B.; Vancso, G. J. Quantitative mapping of elastic moduli at the nanoscale in phase separated polyurethanes by AFM. *Eur. Polym. J.* **2011**, *47*, 692−698.
(48) Sweers, K.; van der Werf, K.; Bennink, M.; Subramaniam, V. Nanomechanical properties of alpha-synuclein amyloid fibrils: a comparative study by nanoindentation, harmonic force microscopy, and peakforce QNM. *Nanoscale Res. Lett.* **2011**, *6*.
(49) Derjaguin, B. V.; Muller, V. M.; Toporov, Y. P. Effect of contact deformations on the adhesion of particles. *J. Colloid Interface Sci.* **1975**, *53*, 314−326.
(50) Gigler, A.; Gnahm, C.; Marti, O.; Schimmel, T.; Walheim, S. Towards quantitative materials characterization with digital pulsed force mode imaging. In *Proceedings of the International Conference on Nanoscience and Technology*, Meyer, E., Hegner, M., Gerber, C., Guntherodt, H. J., Eds.; Iop Publishing Ltd: Bristol, U.K., 2007; Vol. *61*, pp 346−351.
(51) Rezende, C. A.; Lee, L. T.; Galembeck, F. Surface mechanical properties of thin polymer films investigated by AFM in pulsed force mode. *Langmuir* **2009**, *25*, 9938−9946.
(52) Yamanaka, K.; Nakano, S. Quantitative elasticity evaluation by contact resonance in an atomic force microscope. *Appl. Phys. A* **1998**, *66*, S313−S317.
(53) Pittenger, B. *HarmoniX Microscopy for Materials Characterization*. http://nanoscaleworld.bruker-axs.com/pdfs/appnotes/Quantitative-Mechanical-Property-Mapping-at-the-Nanoscale-with-PeakForce-QNM-AN128.pdf
(54) Pittenger, B.; Erina, N.; Su, C. *Quantitative Mechanical Property Mapping at the Nanoscale with PeakForce QNM*. http://www.veeco.com/pdfs/appnotes/quantitative-mechanical-property-mapping-at-the-nanoscale-with-peakforce-qnm-an128-lores.pdf
(55) VanLandingham, M.; Villarrubia, J.; Meyers, G. Recent progress in nanoscale indentation of polymers using the AFM. In *Proceedings of the International Congress on Experimental Mechanics*, June 5−8, 2000, Orlando, FL, Society for Experimental Mechanics: Bethel, CT, 2000; pp 912−915.
(56) Zhang, G.; Liu, Y.; Yuan, Q.; Zong, C.; Liu, J.; Lu, L. Dual modal in vivo imaging using upconversion luminescence and enhanced computed tomography properties. *Nanoscale* **2011**, *3*, 4365−4371.

(57) Tranchida, D.; Kiflie, Z.; Piccarolo, S. Viscoelastic recovery behavior following atomic force microscope nanoindentation of semicrystalline poly(ethylene). *Macromolecules* **2007**, *40*, 7366−7371.
(58) Tranchida, D.; Piccarolo, S.; Loos, J.; Alexeev, A. Accurately evaluating Young's modulus of polymers through nanoindentations: a phenomenological correction factor to the Oliver and Pharr procedure. *Appl. Phys. Lett.* **2006**, *89*.
(59) Tranchida, D.; Piccarolo, S. On the use of the nanoindentation unloading curve to measure the Young's modulus of polymers on a nanometer scale. *Macromol. Rapid Commun.* **2005**, *26*, 1800−1804.
(60) Clifford, C. A.; Seah, M. P. Quantification issues in the identification of nanoscale regions of homopolymers using modulus measurement via AFM nanoindentation. *Appl. Surf. Sci.* **2005**, *252*, 1915−1933.
(61) Withers, J. R.; Aston, D. E. Nanomechanical measurements with AFM in the elastic limit. *Adv. Colloid Interface Sci.* **2006**, *120*, 57−67.
(62) Alderighi, M.; Ierardi, V.; Fuso, F.; Allegrini, M.; Solaro, R. Size effects in nanoindentation of hard and soft surfaces. *Nanotechnology* **2009**, *20*.
(63) Briscoe, B. J.; Sebastian, K. S.; Adams, M. J. The effect of indenter geometry on the elastic response to indentation. *J. Phys. D: Appl. Phys.* **1994**, *27*, 1156−1162.
(64) Napp, J.; Behnke, T.; Fischer, L.; Wurth, C.; Wottawa, M.; Katschinski, D. M.; Alves, F.; Resch-Genger, U.; Schaferling, M. Targeted luminescent near-infrared polymer-nanoprobes for in vivo imaging of tumor hypoxia. *Anal. Chem.* **2011**, *83*, 9039−9046.
(65) Hou, H. Y.; Chang, N. K.; Chang, S. H. Dynamic indentation of polymers using the atomic force microscope. *Nanomech. Mater. Struct.* **2006**, 171−180.
(66) Choi, K. Y.; Yoon, H. Y.; Kim, J. H.; Bae, S. M.; Park, R. W.; Kang, Y. M.; Kim, I. S.; Kwon, I. C.; Choi, K.; Jeong, S. Y.; Kim, K.; Park, J. H. Smart nanocarrier based on PEGylated hyaluronic acid for cancer therapy. *ACS Nano* **2011**, *5*, 8591−8599.
(67) Jiang, X.; Sha, X.; Xin, H.; Chen, L.; Gao, X.; Wang, X.; Law, K.; Gu, J.; Chen, Y.; Jiang, Y.; Ren, X.; Ren, Q.; Fang, X. Self-aggregated pegylated poly (trimethylene carbonate) nanoparticles decorated with c(RGDyK) peptide for targeted paclitaxel delivery to integrin-rich tumors. *Biomaterials* **2011**, *32*, 9457−9469.
(68) Lin, D. C.; Shreiber, D. I.; Dimitriadis, E. K.; Horkay, F. Spherical indentation of soft matter beyond the Hertzian regime: numerical and experimental validation of hyperelastic models. *Biomech. Model Mech.* **2009**, *8*, 345−358.
(69) VanLandingham, M. R.; Villarrubia, J. S.; Guthrie, W. F.; Meyers, G. F. Nanoindentation of polymers: an overview. *Macromol. Symp.* **2001**, *167*, 15−43.
(70) Belikov, S.; Erina, N.; Huang, L.; Su, C. M.; Prater, C.; Magonov, S.; Ginzburg, V.; McIntyre, B.; Lakrout, H.; Meyers, G. Parametrization of atomic force microscopy tip shape models for quantitative nanomechanical measurements. *J. Vac. Sci. Technol., B* **2009**, *27*, 984−992.
(71) Moeller, G. AFM nanoindentation of viscoelastic materials with large end-radius probes. *J. Polym. Sci. Polym. Phys.* **2009**, *47*, 1573−1587.
(72) Johnson, K. L.; Kendall, K.; Roberts, A. D. Surface energy and the contact of elastic solids. *Proc. R. Soc. London, Ser. A* **1971**, *324*, 301−313.
(73) Diaconu, I.; Dorohoi, D. Properties of polyurethane thin films. *J. Optoelectron. Adv. Mater.* **2005**, *7*, 921−924.
(74) Adkins, R. T. *Information Sources in Polymers and Plastics*; Bowker-Saur: London, 1989.
(75) Kalpakjian, S.; Schmid, S. R. *Manufacturing Processes for Engineering Materials*, 5th ed.; Pearson Education: Upper Saddle River, NJ, 2008.
(76) Oliver, W. C.; Pharr, G. M. Measurement of hardness and elastic modulus by instrumented indentation: advances in understanding and refinements to methodology. *J. Mater. Res.* **2004**, *19*, 3−20.
(77) Williams, P. M.; Shakesheff, K. M.; Davies, M. C.; Jackson, D. E.; Roberts, C. J.; Tendler, S. J. B. Blind reconstruction of scanning probe image data. *J. Vac. Sci. Technol., B* **1996**, *14*, 1557−1562.
(78) Levy, R.; Maaloum, M. Measuring the spring constant of atomic force microscope cantilevers: thermal fluctuations and other methods. *Nanotechnology* **2002**, *13*, 33−37.
(79) Hutter, J. L.; Bechhoefer, J. Calibration of atomic-force microscope tips. *Rev. Sci. Instrum.* **1993**, *64*, 1868−1873.
(80) Gates, R. S.; Reitsma, M. G. Precise atomic force microscope cantilever spring constant calibration using a reference cantilever array. *Rev. Sci. Instrum.* **2007**, 78.
(81) Clifford, C. A.; Seah, M. P. The determination of atomic force microscope cantilever spring constants via dimensional methods for nanomechanical analysis. *Nanotechnology* **2005**, *16*, 1666−1680.
(82) Tortonese, M.; Kirk, M. Characterization of application specific probes for SPMs. *Proc. Soc. Photo-Opt. Ins.* **1997**, *3009*, 53−60.
(83) de Abajo, F. J. G.; Aizpurua, J. Numerical simulation of electron energy loss near inhomogeneous dielectrics. *Phys. Rev. B* **1997**, *56*, 15873−15884.
(84) Marti, O.; Barenz, J.; Brunner, R.; Hipp, M.; Hollricher, O.; Horsch, I.; Mlynek, J. Photons and local probes. *NATO Adv. Study Inst. Ser., Ser. E* **1998**, *348*, 155−174.
(85) Levadny, V. G.; Belaya, M. L.; Pink, D. A.; Jericho, M. H. Theory of electrostatic effects in soft biological interfaces using atomic force microscopy. *Biophys. J.* **1996**, *70*, 1745−1752.
(86) King, R. B. Elastic analysis of some punch problems for a layered medium. *Int. J. Solids Struct.* **1987**, *23*, 1657−1664.
(87) Fischer-Cripps, A. C. *Introduction to Contact Mechanics*, 2nd ed.; Springer: New York, 2007.
(88) El-Sayed, A.; Masuda, T.; Akita, H.; Harashima, H. Stearylated INF7 peptide enhances endosomal escape and gene expression of PEGylated nanoparticles both in vitro and in vivo. *J. Pharm. Sci.* **2012**, *101*, 879−882.
(89) Grunlan, J. C.; Xia, X. Y.; Rowenhorst, D.; Gerberich, W. W. Preparation and evaluation of tungsten tips relative to diamond for nanoindentation of soft materials. *Rev. Sci. Instrum.* **2001**, *72*, 2804−2810.
(90) Butt, H.-J.; Kappl, M. *Introduction in Surface and Interfacial Forces*; Wiley-VCH: Weinheim, Germany, 2010.
(91) Grierson, D. S.; Flater, E. E.; Carpick, R. W. Accounting for the JKR-DMT transition in adhesion and friction measurements with atomic force microscopy. *J. Adhes. Sci. Technol.* **2005**, *19*, 291−311.
(92) Tabor, D. Surface forces and surface interactions. *J. Colloid Interface Sci.* **1977**, *58*, 2−13.
(93) Cappella, B.; Dietler, G. Force-distance curves by atomic force microscopy. *Surf. Sci. Rep.* **1999**, *34*, 1−103.
(94) Lin, D. C.; Dmitriadis, E. K.; Horkay, F. Robust strategies for automated AFM force curve analysis-II: adhesion-influenced indentation of soft, elastic materials. *J. Biomech. Eng., Trans. ASME* **2007**, *129*, 904−912.
(95) Lin, D. C.; Dimitriadis, E. K.; Horkay, F. Elasticity of rubber-like materials measured by AFM nanoindentation. *Express Polym. Lett.* **2007**, *1*, 576−584.
(96) Thoreson, E. J.; Martin, J.; Burnham, N. A. The role of few-asperity contacts in adhesion. *J. Colloid Interface Sci.* **2006**, *298*, 94−101.
(97) Ngan, A. H. W.; Tang, B. Viscoelastic effects during unloading in depth-sensing indentation. *J. Mater. Res.* **2002**, *17*, 2604−2610.